INL/JOU-22-70217-Revision-0

Ferroelectric Domain Wall Engineering Enables Thermal Modulation in PMNPT Single Crystals

February 2023

Ankit Negi, Hwang Pill Kim, Anastasia Timofeeva, Yong Zhu, Kara Peters, Divine Kumah, Xiaoning Jiang, Jun Liu, Xuanyi Zhang, Zilong Hua

Changing the World's Energy Future

INL/JOU-22-70217-Revision-0

Ferroelectric Domain Wall Engineering Enables Thermal Modulation in PMNPT Single Crystals

Ankit Negi, Hwang Pill Kim, Anastasia Timofeeva, Yong Zhu, Kara Peters, Divine Kumah, Xiaoning Jiang, Jun Liu, Xuanyi Zhang, Zilong Hua

February 2023

Idaho National Laboratory
Idaho Falls, Idaho 83415

http://www.inl.gov

Prepared for the
U.S. Department of Energy
Under DOE Idaho Operations Office
Contract DE-AC07-05ID14517

ADVANCED MATERIALS
www.advmat.de

Ferroelectric Domain Wall Engineering Enables Thermal Modulation in PMN–PT Single Crystals

*Ankit Negi, Hwang Pill Kim, Zilong Hua, Anastasia Timofeeva, Xuanyi Zhang, Yong Zhu, Kara Peters, Divine Kumah, Xiaoning Jiang, and Jun Liu**

Acting like thermal resistances, ferroelectric domain walls can be manipulated to realize dynamic modulation of thermal conductivity (k), which is essential for developing novel phononic circuits. Despite the interest, little attention has been paid to achieving room-temperature thermal modulation in bulk materials due to challenges in obtaining a high thermal conductivity switching ratio (k_{high}/k_{low}), particularly in commercially viable materials. Here, room-temperature thermal modulation in 2.5 mm-thick $Pb(Mg_{1/3}Nb_{2/3})O_3$–$xPbTiO_3$ (PMN–xPT) single crystals is demonstrated. With the use of advanced poling conditions, assisted by the systematic study on composition and orientation dependence of PMN–xPT, a range of thermal conductivity switching ratios with a maximum of ≈1.27 is observed. Simultaneous measurements of piezoelectric coefficient (d_{33}) to characterize the poling state, domain wall density using polarized light microscopy (PLM), and birefringence change using quantitative PLM reveal that compared to the unpoled state, the domain wall density at intermediate poling states ($0< d_{33}<d_{33,max}$) is lower due to the enlargement in domain size. At optimized poling conditions ($d_{33,max}$), the domain sizes show increased inhomogeneity that leads to enhancement in the domain wall density. This work highlights the potential of commercially available PMN–xPT single crystals among other relaxor-ferroelectrics for achieving temperature control in solid-state devices.

1. Introduction

In recent years, domain wall (DW) engineering in ferroelectric materials has been at the forefront of leading advancements in nanoelectronics, optics, and photovoltaics, often considered as a promising approach to achieve modulation of electrical, magnetic, optical, and thermal properties.[1–3] DWs are interfaces separating regions of different polarization orientations in ferroelectric materials. The structural or polarization discontinuity at DWs results in anomalous behavior in the material compared to the monodomain state. In relaxor-ferroelectrics such as $Pb(Mg_{1/3}Nb_{2/3})O_3$–$PbTiO_3$ (PMN–PT) or $Pb(In_{1/2}Nb_{1/2})O_3$–$Pb(Mg_{1/3}Nb_{2/3})O_3$–$PbTiO_3$ (PIN–PMN–PT), manipulating DWs has been shown to achieve exceptional dielectric and piezoelectric properties, lending them as excellent candidates for several electromechanical applications including sensors, actuators, energy storage, drug delivery, diagnostic imaging, and non-destructive testing.[4–9]

Among several DW engineering methods to achieve further enhancement, the use of alternating current poling (ACP) to manipulate domains has received considerable attention due to its convenience and effectiveness.[10–16] Studies have shown that up to 40% enhancement in piezoelectric coefficient (d_{33}) and 35% enhancement in free dielectric constants using ACP compared to conventional direct current poling (DCP) methods.[10–16] However, even though the DW engineering-based piezoelectric property enhancement is consistent for ACP, a consensus on how the domain size (or DW density) influences the piezoelectric properties is still not reached. Conventional belief in ferroelectrics has been that the property enhancement is due to high domain wall density.[17–19] Studies by Chang et al.,[11] Xu et al.,[16] Zhang et al.,[13] and Sun et al.[10] on PMN–PT single crystals (SCs) show that the presence of monoclinic phases and finer domain sizes as a result of ACP are responsible for piezoelectric property enhancement, indicating that the conventional wisdom still holds for relaxor-ferroelectrics. However,

A. Negi, H. P. Kim, A. Timofeeva, Y. Zhu, K. Peters, X. Jiang, J. Liu
Department of Mechanical and Aerospace Engineering
North Carolina State University
Raleigh, NC 27695, USA
E-mail: jliu38@ncsu.edu

The ORCID identification number(s) for the author(s) of this article can be found under https://doi.org/10.1002/adma.202211286.

DOI: 10.1002/adma.202211286

Z. Hua
Materials Science and Manufacturing department
EES&T
Idaho National laboratory
Idaho Falls, ID 83401, USA

X. Zhang, D. Kumah
Department of Physics
North Carolina State University
Raleigh, NC 27695, USA

other studies have shown conflicting results, suggesting an inverse relationship between domain size and piezoelectric properties.[20] Qiu et al. showed that the enhancement in [001] AC-poled PMN–PT is due to the reduction of 71° DWs.[21] Similar results were also obtained in other studies,[22] including other relaxor-ferroelectrics such as PIN–PMN–PT.[23]

Part of the reason for the conflicting results observed in the literature lies in the limitations of DW density characterization methods. Typical experimental methods used to characterize domains can be classified into electromechanical (piezoresponse force microscopy (PFM)),[11] optical (polarized light microscopy (PLM),[21] and diffraction-based (X-ray diffraction (XRD))[24]) methods. PFM only scans the surface features (depth < 10 nm) and typically over a small region (≈10–50 μm). This localized measurement makes it highly susceptible to skin effects and artifacts in relaxor-ferroelectrics,[25] meaning that the PFM might not reflect the bulk domain structure in crystals. Although PLM does scan the bulk of the crystal, it is only suitable for observing DW density along a certain direction, otherwise, the overlap of domain walls makes it difficult to interpret the PLM data.[26] XRD works well to assess the bulk domain structure but is limited by the selection of refinements, particularly for inhomogeneous domain sizes, which leads to inconsistency in analyzing the XRD data.[27–29] Thus, although localized DW density can be obtained using such characterizations, measurement of bulk domain structures (typically for thicker samples) can involve some uncertainty due to inhomogeneity in the DW distribution. In addition, use of simulation methods such as phase field[21] and first-principles[30] can help identify the mesoscale or atomistic scale origin of piezoelectricity, but does not account for potential inhomogeneity in bulk scale. This challenge highlights the need for a bulk characterization method to assess the overall domain structure in relaxor-ferroelectrics and to understand the influence of DW density on electromechanical property enhancement.

Interestingly, DW engineering has also been applied in the field of thermal science, to modulate thermal conductivity (k) for achieving better control of solid-state heat transfer.[31–39] Thermal conductivity decreases by introducing DWs that act as thermal resistances inhibiting thermal transport.[31–39] The ease in manipulating ferroelectric DW density by electrical input has opened novel possibilities in thermal transport engineering, which led to developments in ferroelectric thermal switches to enable dynamic control over heat flux in a material. Thermal switches modulate thermal conductivity between two states (k_{high} and k_{low}), where the high thermal conductivity state (k_{high}) is a result of lower ferroelectric DW density and vice versa. Several ferroelectric DW-based thermal switches have been reported, attempting to achieve maximum contrast in DW density to obtain a high thermal conductivity switching ratio ($k_{high}/\ k_{low}$).[31–39] Thus, utilizing this well-established relation between thermal conductivity and DW density, thermal conductivity characterization can serve as an alternative approach to assess the bulk DW density in relaxor-ferroelectrics.

However, most thermal switches proposed so far focuses on thin films,[34–39] and less attention has been paid to achieving thermal conductivity modulation in bulk crystals[31–33] despite their practical feasibility. Further, the length scale and orientation of domains in thin films are primarily restricted by the film thickness aside from other factors such as strain, residual stress, and boundary conditions. Thus, achieving a high thermal conductivity modulation (by enhancing contrast in DW density) is challenging. The only solution is to somehow reduce the domain size to sizes comparable to the length scale of heat carriers (phonon mean free path), taking advantage of boundary scattering. But achieving domain size reduction to such scales (usually < 100 nm) requires specific film preparation and high electric field, which has limited the maximum thermal conductivity contrast.[34–39] It poses the question of whether bulk-scale thermal modulation can offer a comparable or even higher thermal contrast, considering the domain size restrictions on bulk samples are less severe. Additionally, while several studies have used a constant voltage bias (i.e., DCP) to manipulate ferroelectric domain walls, there has been little exploration of other electrical poling methods, such as ACP, which may improve the thermal conductivity contrast.

In this regard, we demonstrate thermal conductivity modulation in lead-based relaxor-ferroelectric [001]-oriented $(100–x)Pb(Mg_{1/3}Nb_{2/3})O_3–xPbTiO_3$ (PMN–xPT), ($27<x<33$) single crystals (2.5 mm-thick). The primary reason to choose PMN–PT single crystals is their substantial enhancement in piezoelectric coefficient ($d_{33} > 2000$ pC N^{-1}) using DW engineering near morphotropic phase boundary (MPB: $27<x<32$) compared to other ferroelectrics. In addition, DW engineering of PMN–PT SCs using ACP has been readily conducted and well documented in the literature.[10–16] The purpose of this work is twofold: 1) First, to demonstrate thermal conductivity modulation (or DW density contrast) with DW engineering of PMN–PT SCs using DCP and ACP, which is supported by the DW density measurements using PLM and quantitative PLM (QPLM) based birefringence measurement; 2) Second, to measure the piezoelectric coefficient (d_{33}) for the same set of samples to understand the effect of DW density on the d_{33} enhancement.

2. Results and Discussion

2.1. Thermal Conductivity Modulation for ACP PMN–(≈30–33) PT SCs Poled Along the [001] Direction

Probing the bulk thermal properties of ferroelectric DWs in PMN–PT single crystals is challenging for several reasons. First, the probing depth (thermal penetration depth) in two of the most accurate thermal characterization methods, namely time domain thermo-reflectance (TDTR)[40–42] and frequency domain thermo-reflectance (FDTR),[43] is only a few microns. Considering an average domain size of 1 μm in PMN–PT SCs, these methods can only capture a few domains near the surface that do not reflect the real domain structure inside the material. Another common approach to measure thermal conductivity, the 3ω method,[44] does not apply in this case. The 3ω method requires the deposition of a metal thermometer on top of the sample. This requirement is typically accomplished through lithography, which necessitates baking samples at temperatures greater than 150 °C, higher than the depoling temperature (when the aligned domains begin to reorient) of PMN–PT SCs (≈130–170 °C).[45] Other methods, such as Laser Flash Analysis and HotDisk, have strict requirements on sample

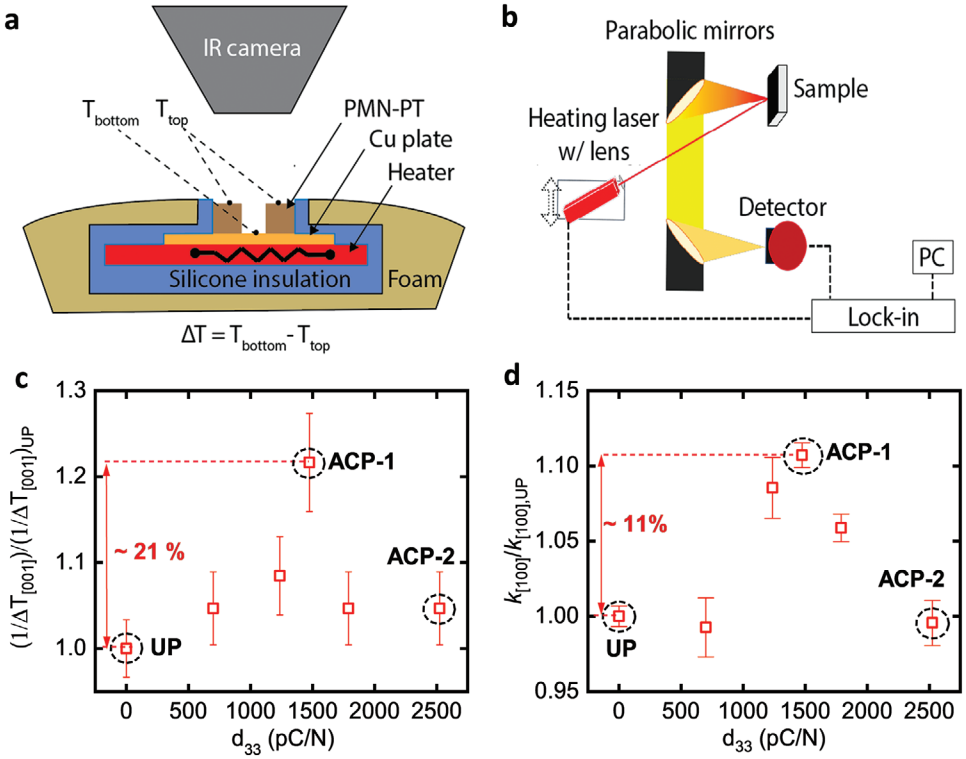

Figure 1. a) Schematic of experimental setup for steady-state temperature difference characterization. The temperature difference ($\Delta T_{[001]}$) across the PMN–PT sample is measured using the IR camera under steady state. b) Schematic of experimental setup for thermal conductivity measurement using PTR. c) Normalized temperature difference $[(1/\Delta T)/(1/\Delta T)_{UP}]$ along the [001] direction of the UP and ACP PMN–(≈30–33) PT single crystals poled along the [001] direction as measured from the steady-state IR measurement. d) The normalized thermal conductivity ($k_{[100]}/k_{[100],UP}$) of UP and ACP PMN–(≈30–33) PT SCs poled along the [001] direction. The sample size for both measurements is 10 mm × 5 mm × 2.5 mm. The data is presented in the form of mean ± standard deviation. Similar behavior of thermal contrast is observed in both results thereby verifying the steady-state measurements.

shape and size, requiring large sample sizes and thicknesses that have a limited frequency range for their transducer applications.[46] Thus, given the need to probe bulk thermal transport in PMN–PT SCs, this work uses a steady-state infrared radiation (IR) camera measurement to obtain the temperature difference across the single crystals (along the [001] direction). **Figure 1**a shows the schematic of the steady-state IR camera method for temperature difference (the details are described in the "Thermal Characterization" part of the Experimental Section). The steady-state IR camera method was calibrated using standard BK-7 glass ($k \approx 1.0$ W m^{-1} K^{-1}) and fused quartz ($k \approx 1.4$ W m^{-1} K^{-1}) samples. These standard samples were selected to ensure that the method is sensitive to small changes in thermal conductivity (thermal conductivity contrast of 40%). Based on the data from previous thermal conductivity studies (refer Section S2, Supporting Information, for more details), the anticipated thermal conductivity contrast is between ≈10%–60%. Further details regarding calibration are provided in Section S3, Supporting Information.

First, we measured the thermal conductivity modulation in ACP ([001] poled) PMN–(≈30–33)PT SCs. All the crystals were initially depoled using the method delineated in the "Sample Description and Poling Conditions" part of the Experimental Section, resulting in an unpoled (UP) state, which corresponds to a $d_{33} \approx 0$ pC N^{-1}. We varied the poling conditions in ACP to obtain a range of poling states (marked by distinct d_{33} values). The poling conditions and measured d_{33} are shown in the "Poling Conditions and Piezoelectric Coefficient" part of the Experiental Section and **Table 1**. The reported thermal conductivity enhancement (or contrast) is measured with reference to the thermal conductivity of the UP state. We anticipated a monotonous thermal conductivity contrast with an increasing d_{33}, under the assumption that the DW density (or domain size) change is primarily responsible for the contrast in d_{33}.[17–20]

Figure 1c shows the normalized temperature difference $[(1/\Delta T)/(1/\Delta T_{UP})]$ along the [001] direction observed using the steady-state IR camera measurement. The absolute temperature difference is provided in Section S4, Supporting Information,

Table 1. PMN–(≈30–33) PT SCs ([001-oriented]) for PTR thermal conductivity and steady-state IR camera temperature difference measurements.

#	Poling	E-field [kV cm^{-1}]	Freq. [Hz]	Cycles	d_{33} [pC N^{-1}]	Capacitance [pF]
1	Unpoled	-	-	-	15 ± 15	532.9
2	AC poled	4	1	10	625 ± 25	660.8
3	AC poled	5	1	1	1225 ± 20	673.2
4	AC poled	5	1	2	1525 ± 25	920.6
5	AC poled	10	1	2	1900 ± 15	1253.0
6	AC poled	10	1	40	2400 ± 25	1623.0

for reference. Under the steady state, the contrast in normalized temperature difference is the same as the normalized thermal conductivity contrast. Hereafter for simplicity, we stick to thermal conductivity in the discussion. Contrary to the assumption, the thermal conductivity does not show a monotonous behavior with an increase in d_{33}. The maximum thermal conductivity enhancement of ≈21% occurs at an intermediate poling state (ACP-1, d_{33}≈ 1480 pC N^{-1}). Intermittent poling states, between UP and ACP-1, show an increase in thermal conductivity with d_{33}. Interestingly, the optimized poling state (ACP-2, d_{33} ≈ 2530 pC N^{-1}) shows a reduced thermal conductivity compared to ACP-1.

We also measured thermal conductivity of the same set of single crystals using the photothermal radiometry (PTR) method (the schematic of the PTR method is in Figure 1b and the description can be found in the "Thermal Characterization" part of the Experimental Section). Figure 1d presents the normalized thermal conductivity ($k_{[100]}/k_{[100],UP}$) along the [100] direction as a function of d_{33}. Thermal conductivity is comparable in both UP and the optimized ACP states, with a maximum value at the intermediate poling state (ACP-1, d_{33} ≈ 1480 pC N^{-1}). This finding is consistent with the results obtained from the steady-state IR camera method. The maximum thermal conductivity enhancement measured using PTR is ≈11%, which is lower than the contrast measured using steady-state IR measurement (≈21%). This discrepancy can be attributed to the fact that PTR measures the in-plane thermal conductivity (along the [100] direction), while steady-state IR measurement is along the cross-plane direction ([001]). Furthermore, our anisotropic temperature difference measurements (shown in **Figure 2** and described in Section 2.2) show that the maximum contrast occurs along the poling direction ([001]), due to different domain structures, which explains the lower thermal conductivity enhancement in PTR compared to the steady-state IR measurement.

Using the inverse dependence of thermal conductivity on DW density, the observations indicate that the DW density decreases with AC poling until ACP-1 and then increases upon further poling. The reduction in DW density for intermediate poling states is consistent with the phase field simulation of Qiu et al. at intermediate E-field (equivalent to intermediate poling state in our case) under ACP that shows an enlargement of domains due to the elimination of 71° DWs.[21] The intermediate poling states offer finer control over thermal conductivity and heat transfer, as opposed to binary k_{high} and k_{low} states in conventional thermal switches. At optimized poling, the domain enlargement behavior is not fully replicated, potentially because of increasing inhomogeneity in the material, where some regions grew smaller while others grew larger, resulting in an overall increase in DW density. The inhomogeneity in the optimized ACP sample is further highlighted in **Figure 3** and discussed in Section 2.3.

It is essential to clarify that even though Figure 1 and Figure 2 show thermal conductivity contrast as a function of

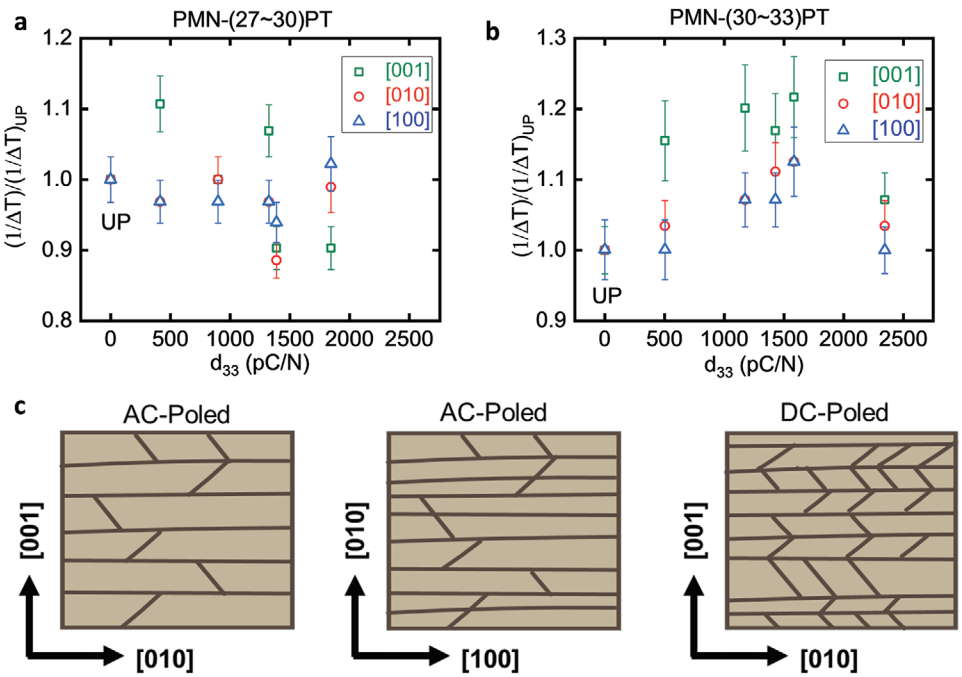

Figure 2. Anisotropic normalized temperature difference [$(1/\Delta T)/(1/\Delta T)_{UP}$)] measured using IR camera for UP, DCP, and ACP PMN–PT SCs. a) PMN–(≈27–30)PT and b) PMN–(≈30–33)PT crystals poled along the [001] direction. The size of single crystals is 2.5 mm × 2.5 mm × 2.5 mm. Each d_{33} value is obtained by poling three samples under similar poling conditions to ensure repeatability. The poling conditions are shown in the "Poling Conditions and Piezoelectric Coefficient" part of the Experimental Section, **Table 2**, and **3**. The data is presented in the form of mean ± standard deviation. c) The schematics of DW orientation under ACP and DCP along the [001] direction. ACP results in laminar domains formed by 109° DWs when viewed along the (100) plane. The majority of 71° DWs are eliminated during ACP leading to a smaller DW density in ACP compared to DCP. The average domain size in the ACP is thus larger than in the DCP. When viewed along the (001) plane for the ACP sample, the overlapping 109° DW makes the domain size smaller.

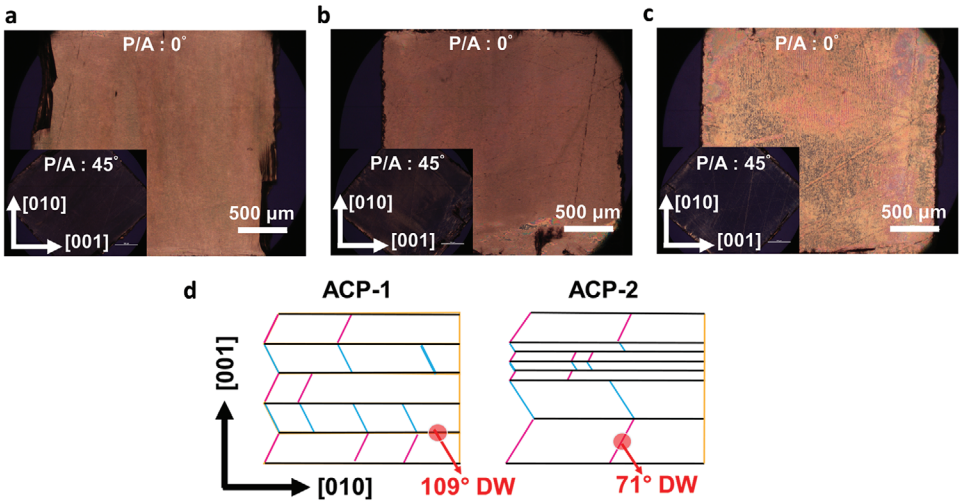

Figure 3. a–c) PLM domain morphology of high-PT PMN–PT SCs at P/A = 0 (inset shows P/A = 45°) for Unpoled (UP) (a), Intermediate AC-poled (ACP-1) along the [001] direction (b), and Optimized AC-poled (ACP-2) along the [001] direction (c). All the crystals were polished down to a thickness of ≈0.2 mm for the PLM measurement. d) The illustration of laminar domains (sandwich between 109° DWs) for the ACP-1 and ACP-2 single crystals poled along the [001] direction. The DW density of 71° DW decreases upon ACP. Based on the PLM observation, the ACP-1 shows homogenous domain size distribution in comparison to ACP-2.

d_{33}, these two parameters are not directly related. Both parameters are related to the DW density, but correlating thermal conductivity and d_{33} is not within the purview of this work. Additionally, we would like to point out that piezoelectric coefficient and thermal conductivity characterization are two separate measurements on the same set of samples. The piezoelectric coefficient serves as a quantifiable parameter to characterize different poling states. The figures are intended to assess the variation in thermal conductivity contrast at different poling states (marked by distinct d_{33} values). Moreover, given the inverse dependence of thermal conductivity on DW density, the figures are also used to highlight the relationship between d_{33} and DW density for PMN–PT single crystals used in this study.

We note that in the current study, the thermal conductivity in PMN–PT single crystals is primarily due to phonons (i.e., lattice vibration) with a negligible electronic contribution. In some ferroelectrics, the formation of charged domain walls can result in metallic-like electrical conductivity,[47–49] which may lead to significant electronic contribution with increasing DW density. However, as described in Section S6, Supporting Information, the poling conditions employed in this study make it unlikely to form such strongly charged domain walls. Furthermore, even if the enhanced electrical conductivity of charged domain walls is considered, the estimated electronic contribution is still negligible compared to the thermal conductivity contrast observed in the study. Moreover, to deconvolute the effect of potential structural changes incurred during ACP on thermal conductivity, we conducted XRD measurements on PMN–(≈30–33)PT single crystals. Section S7, Supporting Information, shows the XRD results of UP, ACP-1, and ACP-2 samples. The peak positions for all the poling states are consistent within the XRD measurement uncertainty, indicating that the effect of any strain on thermal conductivity is similar in all the cases. This suggests that the observed thermal conductivity contrast in the current study is primarily due to the change in DW density with poling.

2.2. Anisotropic Thermal Conductivity Modulation in PMN–PT SCs

To determine the direction that offers the maximum thermal conductivity contrast, we conducted the steady-state temperature difference measurement along all three directions

Table 2. PMN–(≈27–30) PT SCs for anisotropic steady-state temperature difference measurements.

#	Poling	E-field [kV cm^{-1}]	Freq./time [Hz s^{-1}]	Cycles	d_{33} [pC N^{-1}]	Capacitance [pF]
1	Unpoled	-	-	-	15 ± 15	54.0
2	DC poled	1.25	30 s	-	415 ± 15	60.2
3	DC poled	1.25	50 s	-	900 ± 20	80.3
4	DC poled	5	500 s	-	1325 ± 10	112.2
5	AC poled	5	1 Hz	20	1390 ± 15	112.4
6	AC poled	10	1 Hz	20	1845 ± 15	152.7

Table 3. PMN–(≈30–33) PT SCs for anisotropic steady-state temperature difference measurements.

#	Poling	E-field [kV cm^{-1}]	Freq./time [Hz s^{-1}]	Cycles	d_{33} [pC N^{-1}]	Capacitance [pF]
1	Unpoled	-	-	-	20 ± 20	51.6
2	DC poled	1.25	120 s	-	505 ± 15	53.6
3	DC poled	1.25	200 s	-	1175 ± 15	93.5
4	DC poled	5	200 s	-	1430 ± 20	114.6
5	AC poled	5	1 Hz	1	1585 ± 15	126.8
6	AC poled	10	1	20	2345 ± 15	186.0

{001, 010, and 100} for the UP, [001]-poled DCP, and [001]-poled ACP PMN–PT SCs. Figure 2 shows the normalized temperature difference $[(1/\Delta T)/(1/\Delta T)_{UP})]$ measured for PMN–(27–30)PT (low-PT) and PMN–(30–33)PT (high-PT) compositions.

Different thermal modulation behaviors are observed upon poling for the two compositions. The maximum thermal conductivity contrast is achieved at intermediate poling states for both compositions (≈21% at d_{33}≈ 1590 pC N^{-1} for high-PT and ≈12% at d_{33}≈ 1390 pC N^{-1} for low-PT). For low-PT SCs under ACP (Figure 2a), the DW density increases on poling, contrary to the high-PT compositions (Figure 2b), where the DW density decreases in comparison to the UP state. This dissimilarity in thermal conductivity can potentially be explained by the comparatively higher presence of polar nanoregions (PNRs) in low-PT SCs. PNRs serve as regions of phase instability in relaxor-ferroelectrics, which leads to softening of transverse acoustic phonon modes.[50] This explains the lower thermal conductivity of the UP low-PT SC in comparison to high-PT as measured by PTR ($k_{UP,low\text{-}PT}$≈ 1.38 W m^{-1} K^{-1} compared to $k_{UP,high\text{-}PT}$ ≈ 1.43 W m^{-1} K^{-1}). Thus, in low-PT, the thermal conductivity reduction caused by PNRs can outweigh the thermal conductivity increase caused by DW reduction. The inconsistent behavior in the three directions for the low-PT is indicative of asymmetry in lattice dynamics induced by anisotropic PNR structure.[50–52] However, further study is needed to understand this effect. As this study primarily concerns high thermal conductivity contrast, we stick to high-PT crystals for further discussion.

Figure 2b shows the normalized temperature difference along the three directions for DCP and ACP high-PT SCs. The maximum thermal conductivity contrast (≈21%) occurs in the poling direction ([001]). Additionally, the contrast observed in the [010] and [100] directions, which is equivalent in a rhombohedral [001] poled PMN–PT, is similar within the experimental uncertainty. The maximum contrast along these two directions is ≈12%, which is consistent with the PTR measurements shown in Figure 1d. The thermal conductivity of samples increases to a maximum upon poling and then decreases. The trend is particularly evident in [001], where the maximum contrast is higher, but can also be observed along [010] and [100] directions in PMN–(≈30–33)PT single crystals.

The differences in thermal conductivity enhancement between the [001] and [100] (or equivalent [010]) directions can be attributed to the orientation of DWs, as illustrated in Figure 2c. For instance, [001] AC poled sample exhibits laminar-like domains created by the 109° DWs, which are evaluated using PLM (**Figure 4**) and in other studies.[21,53] The same sample shows reduced overall domain size when observed along [100] or [010] directions caused by overlapping 71° and 109° DWs. As shown in Figure 2c, the domain size is maximized along the [001] direction, resulting in the highest thermal conductivity contrast in comparison to other directions.

The maximum thermal conductivity enhancement in ACP samples (≈21%) is higher compared to DCP samples (≈18%), as also shown in Figure S8, Supporting Information. The intermediate poling states (DCP-1 and ACP-1) display the highest enhancement for both poling conditions. The higher contrast in ACP highlights its effectiveness in eliminating the 71° DWs. Additionally, the thermal conductivity contrast between DCP-1 and DCP-2 is significantly lower than ACP samples, which implies that the enhanced inhomogeneity in ACP-2 is related to the switching of electric field direction.

2.3. Domain Wall Density Measured by PLM

To investigate the effect of DW density on piezoelectric enhancement and to further reinforce the thermal conductivity measurement results, we did PLM measurements on PMN–(≈30–33)PT crystals. Figure 3 shows the PLM response of the UP and the ACP samples. Referring to Figure 1c, the intermediate poled state (d_{33}≈ 1480 pC N^{-1}) is called ACP-1, and the optimized poled state (d_{33}≈ 2530 pC N^{-1}) is ACP-2.

Aligning the principal optical axis of single crystals with either that of polarizer or analyzer results in complete extinction.[54] Figure 3a shows extinction at P/A (angle between polarizer and analyzer) = 45° (along {110} directions), which indicates the dominant presence of rhombohedral phase (R-phase).[54] The UP single crystal is expected to be R-phase dominant considering the composition of crystal within the MPB at room temperature. Figure 3b shows that the majority of the regions in ACP-1 are R-phase with small indications of other phases, similar to other studies.[10,55] Figure 3c indicates that ACP-2 is also predominantly R-phase, which implies that the poling conditions do not lead to a significant phase change.

Figure 3d shows a typical domain orientation under ACP of PMN–PT singe crystals, consisting primarily of 109° DWs with a few 71° DWs. The former DWs are birefringent, meaning that light passing through the sample will be retarded depending on the differences in the refractive indices between the fast and slow axis. The retardation of white light results in an interference pattern, as shown in Figure 3a–c at P/A:0°, which is observed using PLM. Higher density of birefringent DWs will result in higher-order interference colors. ACP-1 shows a uniform interference throughout the sample surface, indicating a homogenous domain wall distribution. In contrast, ACP-2 exhibits a mix of higher- and lower-order interference colors. This suggests that some domains grew larger while others shrank, resulting in an inhomogeneous DW distribution in ACP-2, similar to results reported in ref. [56].

Such inhomogeneity in an optimized poling state occurs at a bulk scale (≈mm), which is challenging to observe with localized DW characterization methods. This potentially explains the conflicting results in the studies on domain observation in ACP PMN–PT single crystals. We believe that the continuous polarization reversal during ACP causes inhomogeneous electric field distribution within the material. The ACP-1 underwent ≈1–2 cycles of polarization switching, while ACP-2 underwent 40 cycles under the same electric field. Additionally, as discussed in Section S8, Supporting Information, ACP-2 is more inhomogeneous than DCP-2, indicating inhomogeneity in polarization reversal. Similar inhomogeneity in electric field distribution has been observed in studies involving other ferroelectrics.[57–59] The inherently disordered PMN–PT structure coupled with the large volume of single crystals employed in this study further facilitates the inhomogeneity in polarization reversal.[60,61] Determining the exact cause of inhomogeneity would require a dedicated study involving in situ structural

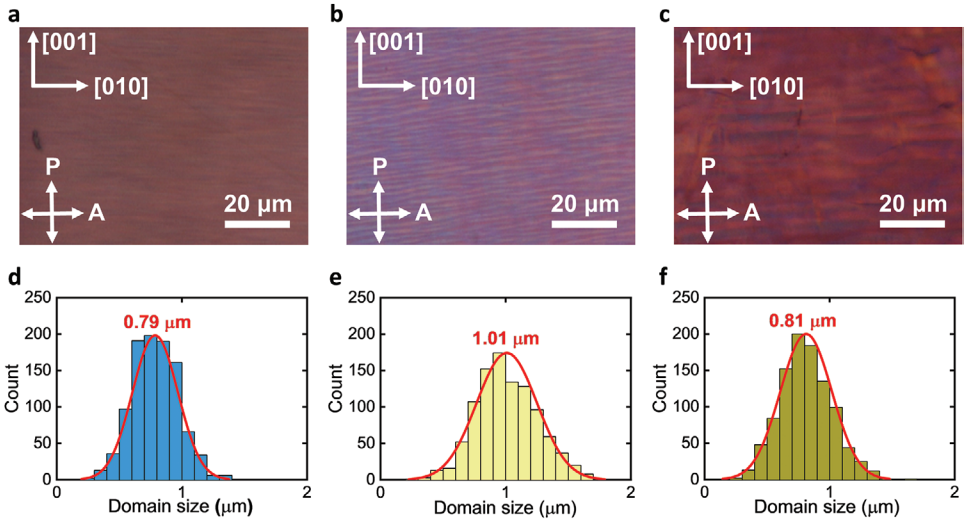

Figure 4. Characterization of domain size for high-PT PMN–PT single crystals. a–c) PLM image examples on the (100) plane for a) UP (a), intermediate ACP along the [001] direction (ACP-1) (b), and optimized ACP along the [001] direction (ACP-2) (c). d–f) Distribution of laminar domain thickness for UP (d), ACP-1 (e), and ACP-2 (f). The distribution is the analysis result from PLM images using three samples from nine different locations.

characterizations, which could be an interesting area for future research.

Next, we calculated the DW density distribution for the UP, ACP-1, and ACP-2 samples. Figure 3d shows that ACP along the [001] direction leads to dominant 109° DWs forming laminar domains. As these 109° DWs are non-overlapping when observed along the (100) plane, the thickness of these laminar domains is a fair estimate for the variation in the domain size with the AC poling. The procedure for calculating the domain size and DW density is described in Section S5, Supporting Information. Figure 4 shows examples of the domain size distribution for the samples measured using PLM under crossed polars (P/A: 90°).

The calculated domain wall density for UP, ACP-1, and ACP-2 samples are $(2.48 \pm 0.10) \times 10^3$, $(1.73 \pm 0.08) \times 10^3$, and $(2.70 \pm 0.25) \times 10^3$ μm^{-1}, respectively. The DW density agrees with the thermal modulation trend in Figure 1c. The UP and ACP-2 sample show similar thermal conductivity and hence a similar DW density. Similarly, ACP-1 shows enhanced thermal conductivity owing to a reduced ferroelectric DW density. Also, the standard deviation in DW density for ACP-2 is much larger than the ACP-1 samples, which again reflects the increased inhomogeneity in domain size distribution. It is important to note that the DW density calculated from PLM for the UP sample only indicates the birefringent DW density, and the actual DW density can be slightly higher than the one calculated here. This also explains the slightly lower UP DW density compared to ACP-2 even though their thermal conductivity is similar.

2.4. Apparent Birefringence Measurement using QPLM

The inhomogeneity observed in ACP-2 (Figure 3c) emphasizes the need for bulk DW density characterization. Localized measurements may lead to smaller or higher DW density values that can lead to incorrect conclusions. To further validate our PLM measurements in the last section, we turn to bulk apparent birefringence measurement of the UP and ACP PMN–(≈30–33) PT samples using the QPLM experimental setup. More information regarding the QPLM is provided in Section S9, Supporting Information. We compared the apparent birefringence of the UP, ACP-1, and ACP-2 samples. Theoretically, birefringence is the measurement of optical retardation in a crystal. The change in birefringence is influenced by the DW density and orientation.[21,53]

Figure 5 shows the retardation maps and corresponding histograms for the UP, ACP-1, and ACP-2 samples. The average retardation (φ) is calculated over a 600 μm × 600 μm area for five different locations in the samples, which is sufficient to scan the bulk of the SC of size 2500 × 2500 μm. Based on φ, the apparent birefringence was calculated using Equation (1) in the "Quantitative Polarized Light Microscopy for Birefringence Characterization" part of the Experimental Section. The average apparent birefringence (Δn) is calculated to be 0.00069 for UP, 0.00057 for ACP-1, and 0.00062 for ACP-2 samples, respectively. In the case of the UP sample, the orientation of DW is random, as also illustrated in Figure 5b,e, where the retardation map shows no specific orientation preference. The net retardation is thus expected to be the highest as compared to the ACP samples. For ACP, the presence of birefringent 109° DW primarily dictates the retardation observed in the samples. Naturally, a higher density of 109° DW will result in higher birefringence. This is exactly what we observed in our QPLM measurements, which indicates that the DW density in the case of ACP-2 is higher than ACP-1. This observation further reinforces the DW density contrast as observed by thermal conductivity modulation and PLM measurements.

We note that the birefringence reported in the QPLM is not the actual birefringence of the material. We measured the apparent birefringence of the samples, which is sensitive to small changes in birefringence between two samples. As the domain wall density changes by around 58% between ACP-1 and ACP-2, leading to an enhancement in thermal conductivity

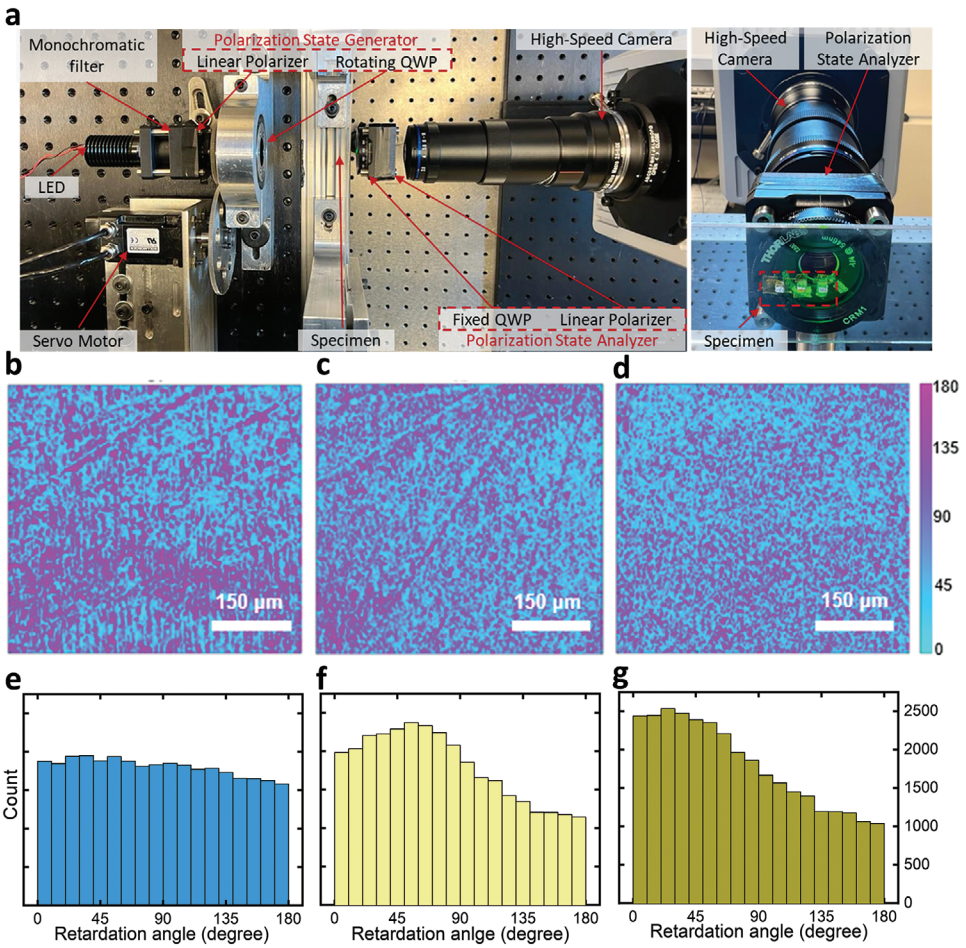

Figure 5. a) Experimental setup of the QPLM measurement. b–d) Retardation maps (in degrees) obtained for UP (b), ACP-1 (c), and ACP-2 (d) PMN–(≈30–33)PT SCs. e–g) The corresponding histograms for the retardation maps are also shown for UP (e), ACP-1 (f), and ACP-2 (g) samples. The retardation maps and histograms were obtained for five locations on the samples and the average alignment degree (φ) value is used to calculate the apparent birefringence for each sample. The thickness of the UP, ACP-1, and ACP-2 samples is measured to be around 0.19, 0.22, and 0.18 mm, respectively.

of 21%, the change in birefringence is also expected to be 58% or even lower. Therefore, QPLM was selected specifically because it is sensitive enough to detect such small changes in birefringence.

2.5. Ex Situ Cyclic Poling–Unpoling Test

Heat loss determination is vital for steady-state measurements to ensure repeatability. In the current setup, the total heat input is divided into four pathways: diffusion in the PMN–PT single crystals, conduction loss into the insulation, convection loss to the ambience, and radiation loss. The total heat loss is calculated by subtracting the heat input from the heat diffused into the PMN–PT samples. The heat input is computed based on resistive heating. The diffused heat is evaluated by taking the thermal conductivity of the PMN–PT sample as measured by PTR and the temperature difference measured by the IR camera.

As we compared ΔT among different states (e.g., UP, ACP-1, ACP-2) in this study, it is vital to ensure that the heat loss is the same in all the measurements. The difference between the total heat loss for the UP (≈3.87 mW) and ACP-1 (≈3.79 mW) is around 2.1%, which is much lower than the observed rise in ΔT (≈21%). Additionally, we conducted an ex situ repeatability test on PMN–(30-33)PT single crystals to validate this claim. We measured the same crystals to eliminate any potential influence of varying compositions. Before the IR camera test, the crystals were taken off the heater and thermally depoled for about two hours. Once completely depoled, the UP samples were re-attached to the heater using silver paste and tested under the IR camera. The samples were then poled and tested in the same way. The poling conditions and measured piezoelectric coefficient are shown in the "Poling Conditions and Piezoelectric Coefficient" part of the Experimental Section and **Table 4**. We conducted this test three times to ensure repeatability. **Figure 6** demonstrates consistent thermal contrast for both ACP and DCP PMN–(30–33)PT SCs. The UP samples show a consistent reduction in thermal conductivity, which indicates that the domains are completely reoriented. The maximum thermal contrast in one of the UP–ACP–UP cycles reaches 27%, and the average is 22% over the three cycles. In the UP–DCP–UP test, the maximum modulation is 25%, with an average of 20%. This test confirms that heat loss is similar throughout

Table 4. PMN–(≈30–33) PT SCs for ex situ poling–unpoling cycling test.

#	Poling	E-field [kV cm^{-1}]	Freq./ time [Hz s^{-1}]	Cycles	d_{33} [pC N^{-1}]
1	Unpoled-cycle 1	-	-	-	10 ± 10
2	Unpoled-cycle 2	-	-	-	10 ± 10
3	Unpoled-cycle 2	-	-	-	15 ± 10
4	AC poled-cycle 1	10	1 Hz	1	1597 ± 73
5	AC poled-cycle 2	10	1 Hz	1	1531 ± 66
6	AC poled-cycle 3	10	1 Hz	1	1545 ± 90
7	DC poled-cycle 1	4	150 s	-	1515 ± 60
8	DC poled-cycle 2	4	150 s	-	1460 ± 43
9	DC poled-cycle 3	4	150 s	-	1481 ± 56

our measurements and highlights the reliability of the relaxor-based ferroelectric thermal switch.

3. Conclusion

We have demonstrated the thermal conductivity modulation in bulk scale (millimeter thick) using ferroelectric PMN–PT SCs. We observed a maximum thermal conductivity enhancement of ≈27% for the PMN–(30–33)PT and ≈12% for the PMN–(27–30) PT SCs using AC poling. The anisotropic steady-state temperature difference measurements suggest that the poling direction exhibits the maximum thermal conductivity modulation (maximum DW density contrast). The DW density measurement using PLM and apparent birefringence measurement using QPLM validate the observed thermal conductivity contrast. The PLM also reveals the increased inhomogeneity in domain size distribution in the [001] AC-poled PMN–(30–33) PT SCs under optimized poling conditions. Comparing the thermal conductivity measurement results with piezoelectric property (d_{33}) enhancement reveals that DW density reaches a minimum at intermediate poling states (characterized by an intermittent d_{33} value: $0< d_{33} <d_{33,max}$). Our observations also indicate that the increasing DW density leads to a higher domain size inhomogeneity, particularly for ACP single crystals. At optimized poling (maximum d_{33}), the inhomogeneity dominates, which results in increased overall DW density compared to intermediate poling states. This study highlights the relevance of thermal conductivity characterization as an alternative tool to understand the variation of domain walls in future ferroelectric studies. From the thermal conductivity modulation perspective, such relaxor-based ferroelectric thermal switches can offer remarkable control over thermal transport in a solid-state device, not limited to only the bipolar ON and OFF states as in conventional switches, with the aid of AC poling. Considering a unit of single crystal produces around 20% reduction in heat transfer coupled with the ease of applying an electric field, an array of single crystals would lead to a considerable reduction in overall heat transfer, ideal for solid-state thermal management applications.

4. Experimental Section

Sample Description and Poling Conditions: The [001]-oriented PMN–(27–30)PT (referred to as low-PT) and PMN–(30–33)PT (referred to as high-PT) SCs, with 200 nm-thick Au electrodes on both surfaces were procured from CTS Corp., IL, USA. The sample dimensions for each test are listed in the "Poling Conditions and Piezoelectric Coefficient" part of the Experimental Section. The samples were heated to 200 °C for 30 min for a fullydepoled state (i.e., unpoled (UP) state) before each poling process. All poling procedures were performed using electric signals generated and amplified by a function generator (Agilent 33250A, Santa Clara, CA, USA) and a high-voltage amplifier (Trek, 609B, New York, NY, USA), respectively. Several electric DC-poling conditions were adopted adjusting the amplitude (0–5 kV cm^{-1}) and duration

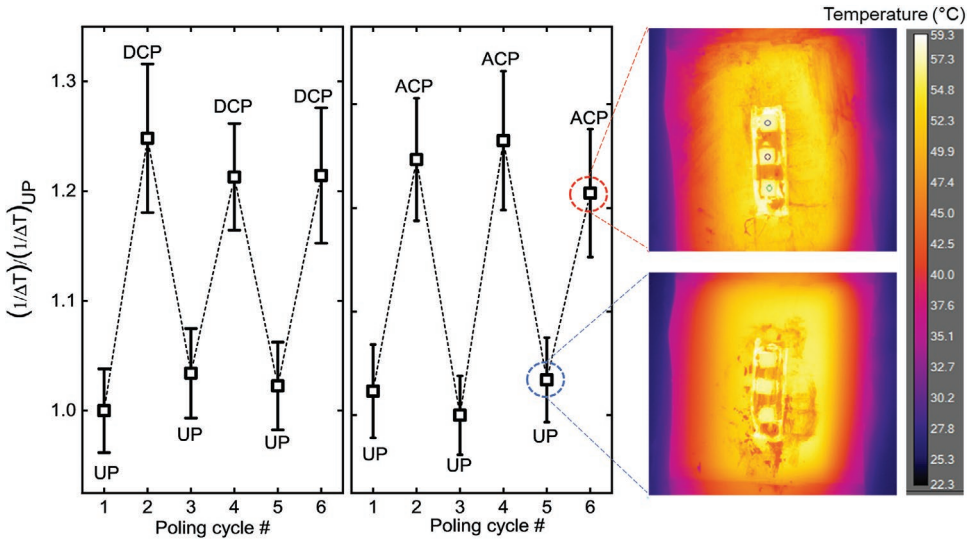

Figure 6. Ex situ cyclic unpoling and poling (ACP and DCP) of PMN–(≈30–33)PT SCs. Left: Cyclic unpoling and DCP test. Middle: Cyclic unpoling and ACP test. Right: IR camera images of the three UP and ACP samples. The plots represent the average temperature difference of the three samples. During each test, the power input to the heater is slightly adjusted to ensure a similar temperature rise. The unpoling and poling test was performed three times to ensure repeatability and confirm similar heat loss throughout the measurements.

time (0–500 s) of the signals. For ACP, continuous bipolar triangular signals were adopted with their waveform parameters controlled. Here, a peak-to-peak amplitude (0–10 kV cm^{-1}) and total induced cycles (0–40 cycles) at 1 Hz were selected as waveform parameters. After poling the crystals, piezoelectric coefficient (d_{33}) and capacitance were measured using a quasi-static piezo d_{33} meter (Model ZJ-4B, Chinese Academy of Science, China) and multifrequency LCR meter (Agilent 4294A, Santa Clara, CA, USA) at 1 kHz, respectively, at room temperature (i.e., 25 °C). Detailed poling conditions in use are listed in the "Poling Conditions and Piezoelectric Coefficient" part of the Experimental Section with their corresponding piezoelectric coefficient (d_{33}) and dielectric permittivity (ε_r). All thermal properties were measured on the bare surfaces [010] and [100] of the materials without electrodes to avoid the effects of the electrodes.

Thermal Characterization: This work used a steady-state infrared radiation (IR) camera measurement to obtain the temperature difference across the single crystals (along the [001] direction) (as shown in Figure 1a). The temperature from the top and bottom of the PMN–PT sample surface was measured using an IR camera. The samples were attached on top of a copper plate that was placed on top of a resistance heater using a thermal adhesive ($k \approx 2$ W m^{-1} K^{-1}). The heater was driven by a DC source. The sample assembly was insulated using silicone ($k \approx 0.2$ W m^{-1} K^{-1}) and foam ($k \approx 0.05$ W m^{-1} K^{-1}) to avoid excessive heat loss to surroundings. The maximum temperature was kept within 60 °C to avoid sample depoling and minimize thermal radiation. Under the steady state, temperature difference ($\Delta T = T_{bottom} - T_{top}$) across the samples was inversely proportional to their thermal conductivity. Thus, the ratio of temperature difference, under the constant heat loss assumption (more details can be found in Section 2.5), should be the same as the thermal conductivity contrast (i.e., $\Delta T_{UP}/\Delta T_{ACP} \approx k_{ACP}/k_{UP}$). Further, to validate the thermal conductivity contrast obtained from steady-state measurements, the PTR method was used to measure the in-plane thermal conductivity (along the [100] direction) of the PMN–(≈30–33)PT SCs as shown in Figure 1b. PTR measures thermal diffusivity of the sample using an intensity-modulated CW laser pump beam and probing the resulting blackbody radiation-induced on the surface. A thin layer of graphite was applied on the sample surface to improve the surface emissivity. The graphite layer thickness was measured using profilometry (≈5 µm), which was insensitive to the fitted thermal diffusivity. Details of the measurement, data analysis, and validation can be found elsewhere.[62]

Polarized Light Microscopy Characterization: The domain characterization was performed using the Eclipse LV100N POL polarized microscope. For the DW density characterization, an additional tint plate (1λ) was used to increase the domain contrast. The samples were polished down to a thickness of ≈0.2 mm for the measurements using diamond lapping films, with 30 µm grit size for coarse polishing and 1 µm for fine polishing.

Quantitative Polarized Light Microscopy for Birefringence Characterization: The quantitative polarized light microscopy (QPLM) setup for the apparent birefringence measurements of the PMN–PT SCs was based on the work of references.[63–65] The specimen was illuminated with a monochromatic green LED light source that was first filtered with a narrow band (10±2 nm) wavelength filter centered at 546.1±2 nm (10MLF10-546, Newport). Linear polarizers for the wavelength range of 480–550 nm, (LPVISA050, ThorLabs) and quarter waveplates (QWP) designed for 546 nm (WPQ05M-546, ThorLabs) were used to generate and analyze polarized light entering and exiting the sample. A high-speed camera (Photron FASTCAM SA-X2) with a 25 mm macro lens (Laowa 25 mm f/2.8 2.5-5X Ultra Macro Lens) was used to record the intensity images at a rate of 250 frames per second. The first QWP was rotated at a constant speed of 105 RPM by a high-speed servo motor (Kollmorgen AKM11B), controlled using a Kollmorgen AKD-T00306 drive with its built-in PID speed control system. All QWP alignment angles were set with respect to the horizontal direction. The method described here[63] was used for calibration of the QWPs. The samples were fixed to a poly(methyl methacrylate) (PMMA) sheet with cut out square holes for the polarized light to travel through. The PMMA was only used as a fixture for the samples and had no effect on the results of the measurements. A harmonic image analysis[63] for images collected over 180° of QWP rotation was used to calculate the alignment and retardation values of each pixel in the sample. The apparent birefringence (Δn) was then calculated using Equation (1),

$$\Delta n = \frac{\phi\lambda}{2\pi t} \tag{1}$$

where ϕ is the retardation in radians, λ is the wavelength of the light propagating through the specimen (546 nm), and t is the thickness of the sample in nm.

Poling Conditions and Piezoelectric Coefficient: Here the sample sizes, poling conditions, and properties at different poled states are described. Three samples were poled for each condition and the average data is presented in the tables. The sample sizes were 10 mm × 5 mm × 2.5 mm for the PTR thermal conductivity and steady-state IR measurements (Figure 1c,d). For the rest of the measurements (Figure 2 and Figure 6), the sample sizes were 2.5 mm × 2.5 mm × 2.5 mm. The samples were poled along the thickness (2.5 mm) direction [001].

Statistical Analysis: The reciprocal of temperature difference ($1/\Delta T$) was normalized with the value of the unpoled samples [$(1/\Delta T)/(1/\Delta T)_{UP}$] as shown in Figure 1c, Figure 2a, Figure 2b, and Figure 6. The data in the mentioned figures were represented in the form of mean ± standard deviation ($n = 3$). The histogram plots in Figure 4d–f were fitted with a normal distribution in the software Origin. The mean value of the normal distribution was presented in the plots. The data for DW density was presented in the form of mean ± standard deviation (n = 9).

Supporting Information

Supporting Information is available from the Wiley Online Library or from the author.

Acknowledgements

The authors would like to thank Shuang Wu from Dr. Y.Z.'s lab for the help with IR camera setup. A.N., X.Z., D.K., X.J., and J.L. acknowledge financial support from the National Science Foundation under the award No. DMR 2011978. H.K. and X.J. acknowledge that this work was supported in part by the Office of Naval Research (ONR) under Grant N00014-21-1-2058. Work performed by Z.H. was supported through the INL Laboratory Directed Research& Development (LDRD) Program under DOE Idaho Operations Office Contract DE-AC07-05ID14517.

Conflict of Interest

The authors declare no conflict of interest.

Data Availability Statement

The data that support the findings of this study are available from the corresponding author upon reasonable request.

Keywords

domain walls, ferroelectrics, poling, thermal conductivity, thermal modulation

Received: December 2, 2022
Revised: February 11, 2023
Published online: April 27, 2023

[1] P. Sharma, T. S. Moise, L. Colombo, J. Seidel, *Adv. Funct. Mater.* **2022**, *32*, 2110263.
[2] S. S. P. Parkin, M. Hayashi, L. Thomas, *Science* **2008**, *320*, 190.
[3] G. Catalan, J. Seidel, R. Ramesh, J. F. Scott, *Rev. Mod. Phys.* **2012**, *84*, 119.
[4] H. P. Kim, H. Wan, C. Luo, Y. Sun, Y. Yamashita, T. Karaki, H. Y. Lee, X. Jiang, *IEEE Trans. Ultrason. Ferroelectr. Freq. Control* **2022**, *69*, 3037.
[5] S. Zhang, F. Li, *J. Appl. Phys.* **2012**, *111*, 031301.
[6] E. Sun, W. Cao, *Prog. Mater. Sci.* **2014**, *65*, 124.
[7] S. Zhang, F. Li, X. Jiang, J. Kim, J. Luo, X. Geng, *Prog. Mater. Sci.* **2015**, *68*, 1.
[8] S. Zhang, F. Li, F. Yu, X. Jiang, H. Y. Lee, J. Luo, T. R. Shrout, *J. Korean Ceram. Soc.* **2018**, *55*, 419.
[9] Y. Yamashita, T. Karaki, H. Y. Lee, H. Wan, H. P. Kim, X. Jiang, *IEEE Trans. Ultrason. Ferroelectr. Freq. Control* **2022**, *69*, 3048.
[10] Y. Sun, T. Karaki, T. Fujii, Y. Yamashita, *Jpn. J. Appl. Phys.* **2019**, *58*, SLLC06.
[11] W. Chang, C. Chung, C. Luo, T. Kim, J. L. Jones, X. Jiang, *Mater. Res. Lett.* **2018**, *6*, 537.
[12] C. Qiu, J. Liu, F. Li, Z. Xu, *J. Appl. Phys.* **2019**, *125*, 014102.
[13] Z. Zhang, J. Xu, L. Yang, S. Liu, J. Xiao, R. Zhu, X. Li, X. Wang, H. Luo, *J. Appl. Phys.* **2019**, *125*, 034104.
[14] J. Liu, C. Qiu, L. Qiao, K. Song, H. Guo, Z. Xu, F. Li, *J. Appl. Phys.* **2020**, *128*, 094104.
[15] H. Wan, C. Luo, C. C. Chung, Y. Yamashita, X. Jiang, *Appl. Phys. Lett.* **2021**, *118*, 102904.
[16] J. Xu, H. Deng, Z. Zeng, Z. Zhang, K. Zhao, J. Chen, N. Nakamori, F. Wang, J. Ma, X. Li, H. Luo, *Appl. Phys. Lett.* **2018**, *112*, 182901.
[17] S. Wada, K. Yako, K. Yokoo, H. Kakemoto, T. Tsurumi, *Ferroelectrics* **2006**, *334*, 17.
[18] R. Ahluwalia, T. Lookman, A. Saxena, W. Cao, *Phys. Rev. B: Condens. Matter Mater. Phys.* **2005**, *72*, 014112.
[19] J. Hlinka, P. Ondrejkovic, P. Marton, *Nanotechnology* **2009**, *20*, 105709.
[20] B. Wang, F. Li, L. Q. Chen, *Adv. Mater.* **2021**, *33*, 2105071.
[21] C. Qiu, B. Wang, N. Zhang, S. Zhang, J. Liu, D. Walker, Y. Wang, H. Tian, T. R. Shrout, Z. Xu, L. Q. Chen, F. Li, *Nature* **2020**, *577*, 350.
[22] H. Wan, C. Luo, C. Liu, W. Y. Chang, Y. Yamashita, X. Jiang, *Acta Mater.* **2021**, *208*, 116759.
[23] A. D. Ushakov, Q. Hu, X. Liu, Z. Xu, X. Wei, V. Y. Shur, *Appl. Phys. Lett.* **2021**, *118*, 232901.
[24] C. Qiu, Z. Xu, Z. An, J. Liu, G. Zhang, S. Zhang, L. Q. Chen, N. Zhang, F. Li, *Acta Mater.* **2021**, *210*, 116853.
[25] G. Xu, P. M. Gehring, C. Stock, K. Conlon, *Phase Transitions* **2006**, *79*, 135.
[26] C. Xu, Q. Li, Q. Yan, N. Luo, Y. Zhang, X. Chu, *J. Am. Ceram. Soc.* **2016**, *99*, 2096.
[27] D. Hou, T. M. Usher, L. Fulanovic, M. Vrabelj, M. Otonicar, H. Ursic, B. Malic, I. Levin, J. L. Jones, *Phys. Rev. B* **2018**, *97*, 214102.
[28] H. Liu, J. Chen, H. Huang, L. Fan, Y. Ren, Z. Pan, J. Deng, L. Q. Chen, X. Xing, *Phys. Rev. Lett.* **2018**, *120*, 55501.
[29] L. Fan, J. Chen, Y. Ren, Z. Pan, L. Zhang, X. Xing, *Phys. Rev. Lett.* **2016**, *116*, 027601.
[30] C. Li, B. Xu, D. Lin, S. Zhang, L. Bellaiche, T. R. Shrout, F. Li, *Phys. Rev. B* **2020**, *101*, 140102.
[31] A. J. H. Mante, J. Volger, *Physica* **1971**, *52*, 577.
[32] M. A. Weilert, M. E. Msall, A. C. Anderson, J. P. Wolfe, *Phys. Rev. Lett.* **1993**, *71*, 735.
[33] M. A. Weilert, M. E. Msall, J. P. Wolfe, A. C. Anderson, *Z. Phys. B* **1993**, *91*, 179.
[34] E. Langenberg, D. Saha, M. E. Holtz, J. J. Wang, D. Bugallo, E. Ferreiro-Vila, H. Paik, I. Hanke, S. Ganschow, D. A. Muller, L. Q. Chen, G. Catalan, N. Domingo, J. Malen, D. G. Schlom, F. Rivadulla, *Nano Lett.* **2019**, *19*, 7901.
[35] J. F. Ihlefeld, B. M. Foley, D. A. Scrymgeour, J. R. Michael, B. B. McKenzie, D. L. Medlin, M. Wallace, S. Trolier-Mckinstry, P. E. Hopkins, *Nano Lett.* **2015**, *15*, 1791.
[36] B. M. Foley, M. Wallace, J. T. Gaskins, E. A. Paisley, R. L. Johnson-Wilke, J. W. Kim, P. J. Ryan, S. Trolier-Mckinstry, P. E. Hopkins, J. F. Ihlefeld, *ACS Appl. Mater. Interfaces* **2018**, *10*, 25493.
[37] J. J. Wang, Y. Wang, J. F. Ihlefeld, P. E. Hopkins, L. Q. Chen, *Acta Mater.* **2016**, *111*, 220.
[38] J. A. Seijas-Bellido, C. Escorihuela-Sayalero, M. Royo, M. P. Ljungberg, J. C. Wojdeł, J. Íñiguez, R. Rurali, *Phys. Rev. B* **2017**, *96*, 140101.
[39] D. Bugallo, E. Langenberg, E. Ferreiro-Vila, E. H. Smith, C. Stefani, X. Batlle, G. Catalan, N. Domingo, D. G. Schlom, F. Rivadulla, *ACS Appl. Mater. Interfaces* **2021**, *13*, 45679.
[40] D. G. Cahill, *Rev. Sci. Instrum.* **2004**, *75*, 5119.
[41] J. Zhu, D. Tang, W. Wang, J. Liu, K. W. Holub, R. Yang, *J. Appl. Phys.* **2010**, *108*, 094315.
[42] J. Liu, J. Zhu, M. Tian, X. Gu, A. Schmidt, R. Yang, *Rev. Sci. Instrum.* **2013**, *84*, 034902.
[43] A. J. Schmidt, R. Cheaito, M. Chiesa, *Rev. Sci. Instrum.* **2009**, *80*, 094901.
[44] H. Wang, M. Sen, *Int. J. Heat Mass Transfer* **2009**, *52*, 2102.
[45] S. Zhang, F. Li, N. P. Sherlock, J. Luo, H. Jae Lee, R. Xia, R. J. Meyer, W. Hackenberger, T. R. Shrout, *J. Cryst. Growth* **2011**, *318*, 846.
[46] C. Dames, *Annu. Rev. Heat Transfer* **2013**, *16*, 7.
[47] G. F. Nataf, M. Guennou, J. M. Gregg, D. Meier, J. Hlinka, E. K. H. Salje, J. Kreisel, *Nat. Rev. Phys.* **2020**, *2*, 634.
[48] P. S. Bednyakov, B. I. Sturman, T. Sluka, A. K. Tagantsev, P. V. Yudin, *npj Comput. Mater.* **2018**, *4*, 65.
[49] T. Sluka, A. K. Tagantsev, P. Bednyakov, N. Setter, *Nat. Commun.* **2013**, *4*, 1808.
[50] G. Xu, J. Wen, C. Stock, P. M. Gehring, *Nat. Mater.* **2008**, *7*, 562.
[51] G. Xu, Z. Zhong, H. Hiraka, G. Shirane, *Phys. Rev. B: Condens. Matter Mater. Phys.* **2004**, *70*, 064107.
[52] F. Li, S. Zhang, T. Yang, Z. Xu, N. Zhang, G. Liu, J. Wang, J. Wang, Z. Cheng, Z. G. Ye, J. Luo, T. R. Shrout, L. Q. Chen, *Nat. Commun.* **2016**, *7*, 13807.
[53] C. Deng, L. Ye, C. He, G. Xu, Q. Zhai, H. Luo, Y. Liu, A. J. Bell, *Adv. Mater.* **2021**, *33*, 2103013.
[54] Z. G. Ye, M. Dong, *J. Appl. Phys.* **2000**, *87*, 2312.
[55] C. Luo, W. Y. Chang, M. Gao, C. H. Chang, J. Li, D. Viehland, J. Tian, X. Jiang, *Acta Mater.* **2020**, *182*, 10.
[56] O. Vlasin, B. Casals, N. Dix, D. Gutiérrez, F. Sánchez, G. Herranz, *Sci. Rep.* **2015**, *5*, 15800.
[57] K. Matyjasek, K. Wolska, R. Z. Rogowski, S. M. Kaczmarek, L. I. Ivleva, *Ferroelectrics* **2011**, *413*, 311.
[58] J. Zhao, S. D. Funni, E. R. Molina, E. C. Dickey, J. L. Jones, *Acta Mater.* **2022**, *226*, 117682.
[59] Y. A. Genenko, J. Glaum, M. J. Hoffmann, K. Albe, *Mater. Sci. Eng. B* **2015**, *192*, 52.
[60] M. S. Song, K. C. Lee, J. C. Choi, K. Lee, S. C. Chae, *Phys. Rev. Mater.* **2021**, *5*, 114408.
[61] X. Wang, Z. Xu, Z. Li, H. Chen, *Solid State Commun.* **2010**, *150*, 1425.
[62] Z. Hua, R. Schley, D. Hurley, *Rev. Sci. Instrum.* **2022**, *93*, 044903.
[63] T. T. Tower, R. T. Tranquillo, *Biophys. J.* **2001**, *81*, 2964.
[64] X. Wu, M. Pankow, H. Y. Shadow Huang, K. Peters, *Meas. Sci. Technol.* **2018**, *29*, 015203.
[65] X. Wu, M. Pankow, H.-Y. S. Huang, K. Peters, *J. Biomed. Opt.* **2018**, *23*, 116002.